Supplement of Biogeosciences, 23, 1497–1514, 2026
https://doi.org/10.5194/bg-23-1497-2026-supplement

Biogeosciences Open Access EGU

Supplement of

Wintertime production and storage of methane in thermokarst ponds of subarctic Norway

Anfisa Pismeniuk et al.

Correspondence to: Anfisa Pismeniuk (anfisa.pismeniuk@geo.uio.no)

S1 Study area

S1.1. Thermokarst pond formation age

We identified the formation age of each studied pond (Sect 2.2, main text) using geo-referenced historical aerial images 1955, 1958, 2003 and 2013 by the Norwegian Mapping Authority and drone imagery (September 2015, September 2020, and September 2023) obtained by the Drone Infrastructure Lab, University of Oslo (Fig. S1–S3). The thermokarst pond formation age was identified as the time of permafrost collapse and not the start of water accumulation (Sect 3.7, main text), as demonstrated in the case of pond A4 (Fig. S1). In pond A4, the permafrost started to collapse in 2013, and the pond was already established by 2020. We used 2023 as the baseline year for age estimation.

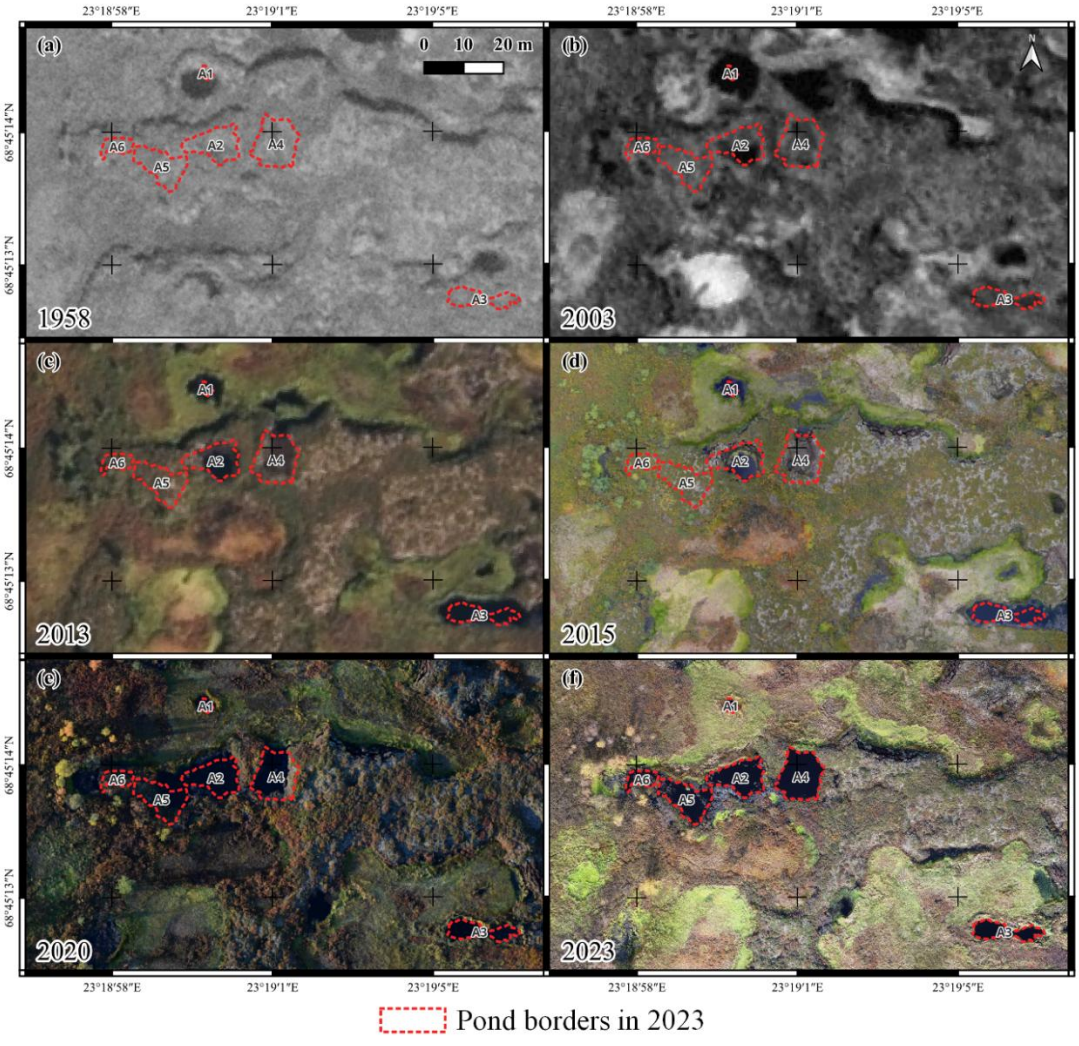

Figure S1. Aerial images of the main study area in Áidejávri (A1-A6) from 1958 to 2023 illustrate the degradation of the peat plateau. The aerial images from 1958 (a), 2003 (b) and 2013 (c) were obtained from the Norwegian Mapping Authority (Norgeibilder.no, 2025), while orthophotos from 2015 (d), 2020 (e), and 2023 (f) were made through drone surveys and processed following the method described in Martin et al., 2021.

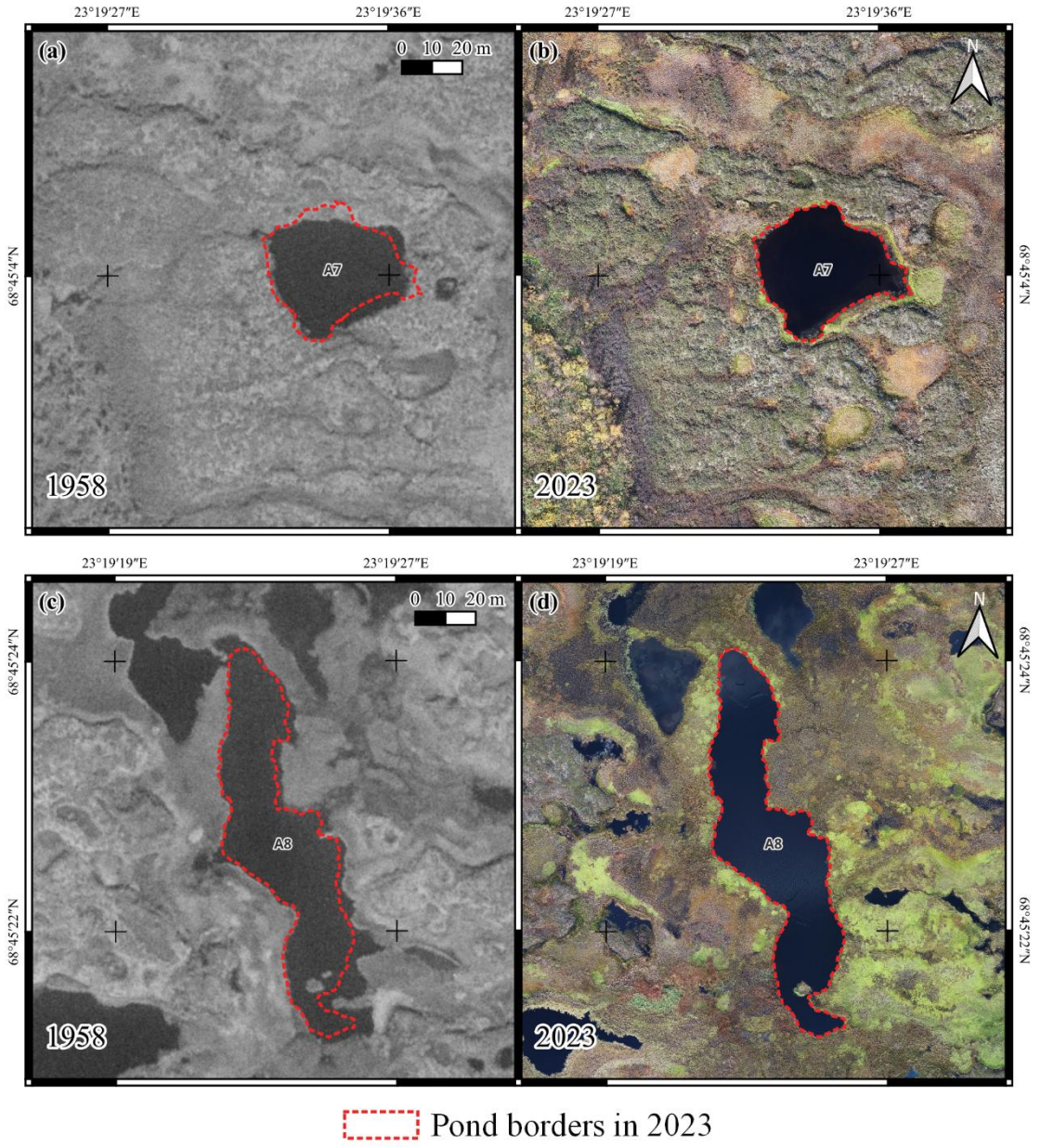

Figure S2. Aerial images of the thermokarst pond A7 (a-b) and non-thermokarst pond A8 (c-d) in 1958 and 2023. The aerial image from 1958 (a and c) was obtained from the Norwegian Mapping Authority (Norgeibilder.no, 2025), while orthophotos from 2023 (b and d) was taken by drone and processed following the method described in Martin et al., 2021.

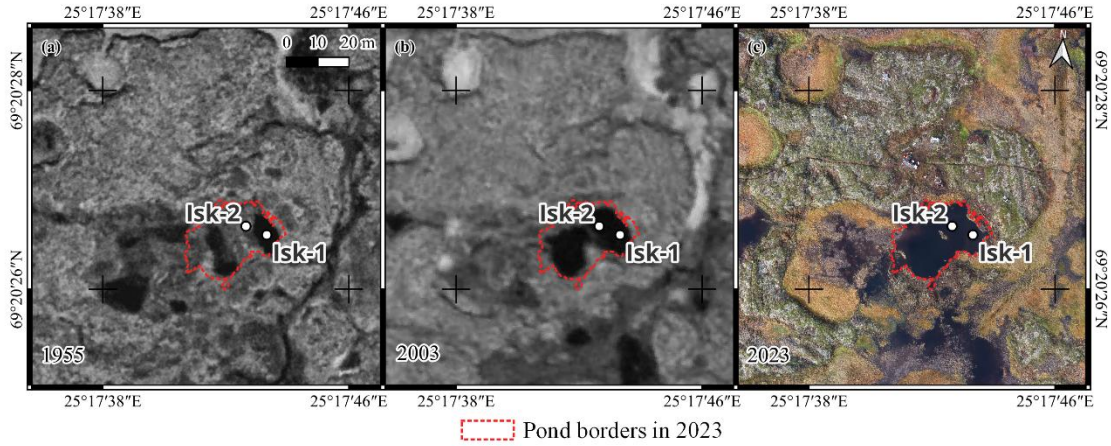

Figure S3. Aerial images of the Iškoras pond (a-c) in 1955 and 2023. The aerial images from 1955 and 2003 (a and b) were obtained from the Norwegian Mapping Authority (Kartverket survey WF-688 H-13 and Norgeibilder.no, 2025), while orthophotos from 2023 (b and d) were taken by drone and processed following the method described in Martin et al., 2021.

S1.2. Pond water temperature

Water temperature in the Iškoras pond was measured using iButton (© Maxim) temperature loggers installed at two depths: 0.6 m (bottom) and 0.4 m. The iButtons (model DS1922L) have an operating range of −40 to +85°C, with a numerical resolution of 0.0625°C and an accuracy of ±0.5°C (Maxim Integrated, 2015). The measurements indicate that the pond was well mixed during the ice-free period (Fig. S4). In winter, temperatures at the two depths differed due to ice formation reaching the upper logger, but the differences did not exceed 2°C (Sect. 3.1, main text).

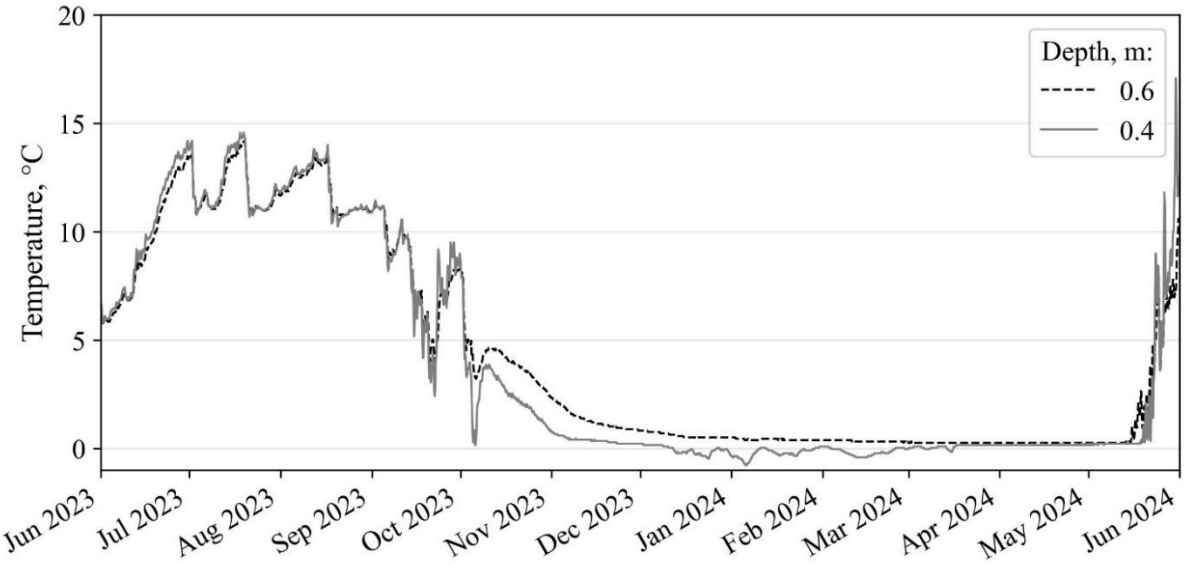

Figure S4. Water temperature measured in Iškoras pond at two depths: 0.4 m and 0.6 m (bottom). Temperatures were recorded using automatic data loggers (iButton).

S1.3. Ice formation and melting season

The studied ponds are ice-covered for nearly eight months. The timing of ice formation (Sect. 3.6, main text) was identified using meteorological data and Sentinel-2 imagery. At Iškoras in 2023, ice growth began between 1–2 October, coinciding with the first substantial air-temperature drop (Fig. S5). At Áidejávri, ice formation started between 6–13 October based on data from the Sihccajávri station and Sentinel-2 (Fig. S6). Ice melt was defined using Sentinel-2 imagery for Áidejávri and temperature loggers in the Iškoras pond (Sect. S1.2). Ice cover persisted until mid-May 2024 and disappeared by late May (Fig. S7).

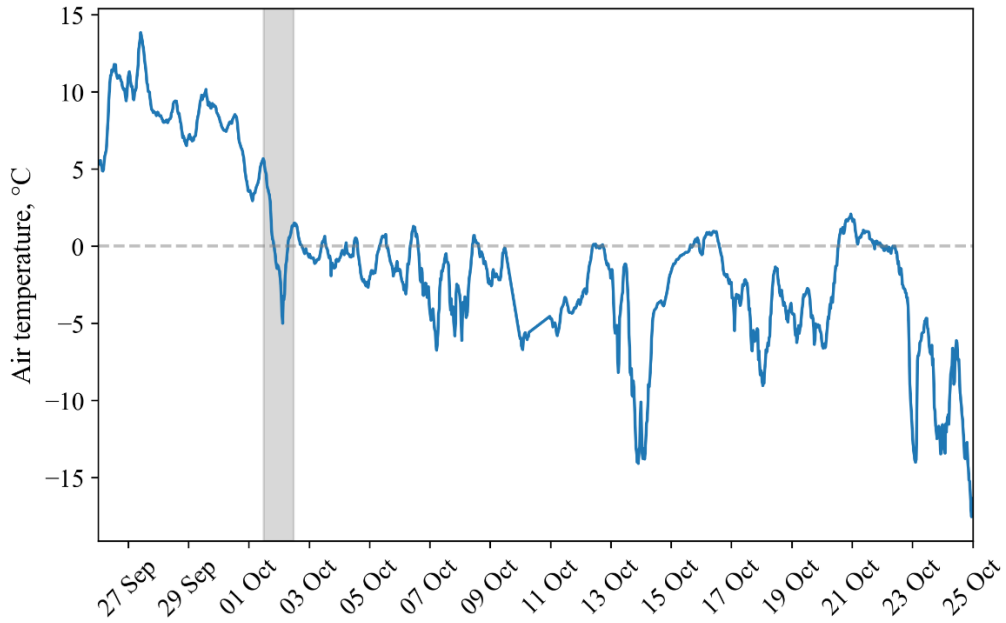

Figure S5. Air temperature measured from September 26, 2023, to October 25, 2023, using a resistance temperature detector (PT-100) located in a radiation shield at 2 m above ground level (a.g.l.) on the eddy covariance tower in Iškoras (Pirk et al., 2024). The beginning of ice formation in 2023 is shown with grey shading.

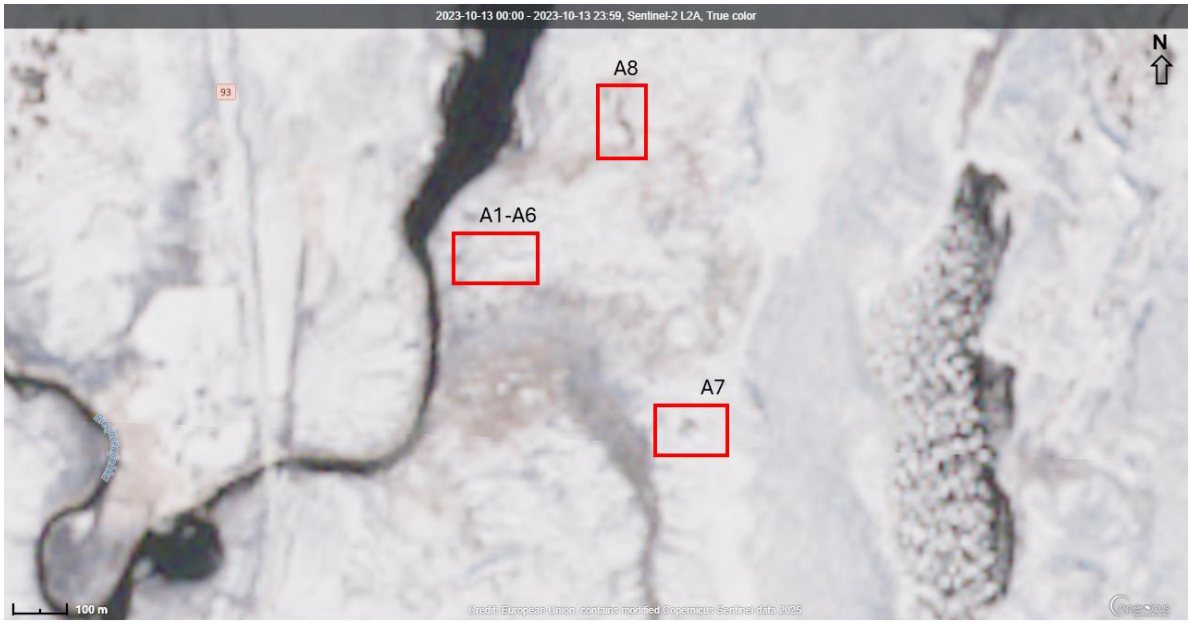

Figure S6. Sentinel-2 L2A image of the Áidejávri area taken on October 13, 2023, from Copernicus Data Browser, https://browser.dataspace.copernicus.eu/ (last access: 15 May 2025). The studied ponds in Áidejávri are indicated with red rectangles. The image shows that, by October 13, the ponds in Áidejávri were ice-covered.

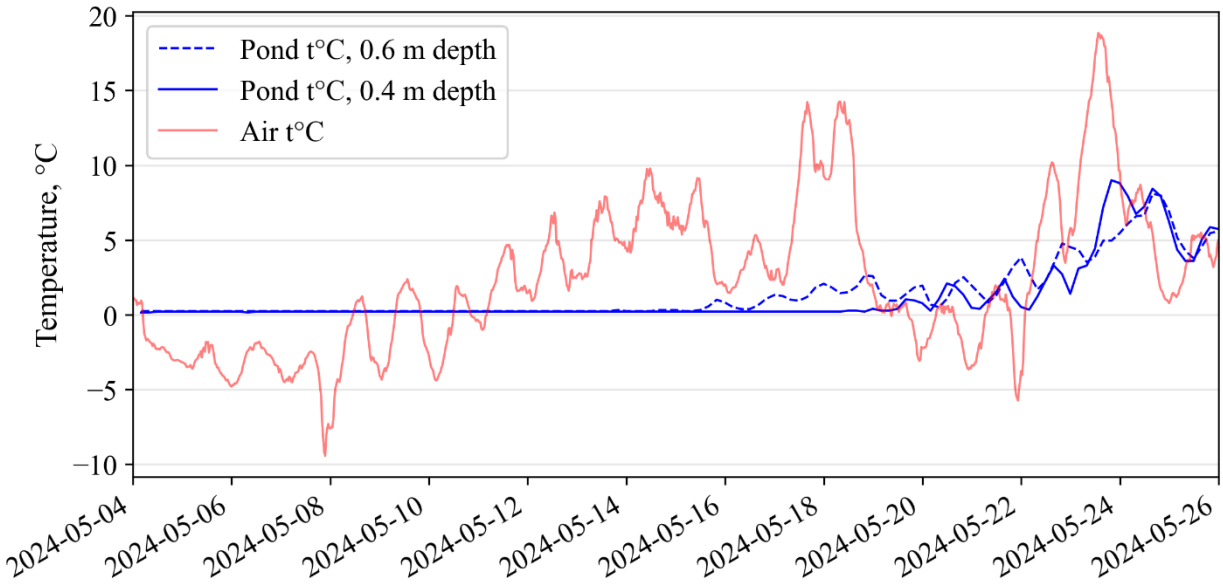

Figure S7. Air and water temperatures of the pond at Iškoras measured between May 4 and May 26, 2024. Water temperatures were recorded using automatic data loggers (iButton) at two depths: 0.4 m and 0.6 m (bottom). Air temperature was measured with a resistance temperature detector (PT-100) located in a radiation shield at 2 m above ground level (a.g.l.) on the eddy covariance tower in Iškoras (Pirk et al., 2024).

S2 Ancillary data

S2.1. Dissolved O_2 and CO_2 concentrations in the studied ponds

Dissolved O_2 (Fig. S8) and CO_2 (Fig. S9a) concentrations were measured alongside CH_4 using the acidified headspace method (Åberg and Wallin, 2014) following the protocol of Knutson et al. (2025). Dissolved CO_2 concentrations in the ponds were calculated from total DIC concentrations after acidification using in situ pH and equilibrium constants adjusted for the pond temperature (Åberg and Wallin, 2014).

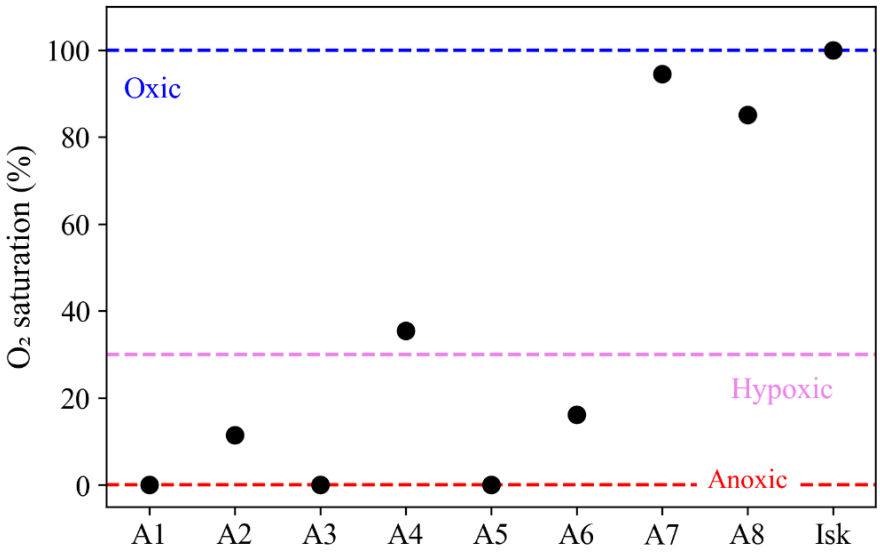

Figure S8. O_2 saturation in surface water during September 2024 relative to atmospheric equilibrium. O_2 conditions are classified as oxic (more than 30 %), hypoxic (below 30 %), and as anoxic when saturation values were below 1 %. We estimated a high absolute error of 20 % in O_2 saturation measurements due to significant differences observed between measured values in replicate samples (Sect. 3.3, main text).

CO_2 concentrations in all seasons exceeded atmospheric values. Similar to DOC and CH_4, a strongly negative correlation was observed between pond size and concentrations of both CO_2 ($p < 0.05$) in September 2024. CO_2 concentrations measured in September were significantly lower in large thermokarst ponds (Isk1/2 and A7 ponds), averaging 30 µM (Fig. S9a). The highest dissolved CO_2 concentrations in September were recorded in the thermokarst ponds experiencing sedge succession A1 and A3, with concentrations of 1735 and 1888 µM, respectively. Although ponds A2, A4, A5, and A6 were to some extent hydrologically connected, they differed in dissolved concentrations of CO_2 concentrations in September which ranged from 421 µM in pond A4 to 986 µM in pond A5 (Fig. S9a). Dissolved CO_2 concentrations increased rapidly with the start of the ice formation in October, in some ponds increasing by an order of magnitude, e.g. in the Isk pond (Fig. S9a). Winter CO_2 concentrations ranged from 2711 µM in pond A3 to 4825 µM in pond A4 (Fig. S9a). All ponds exhibited CO_2:CH_4 ratio higher than 1 (Fig. S9b).

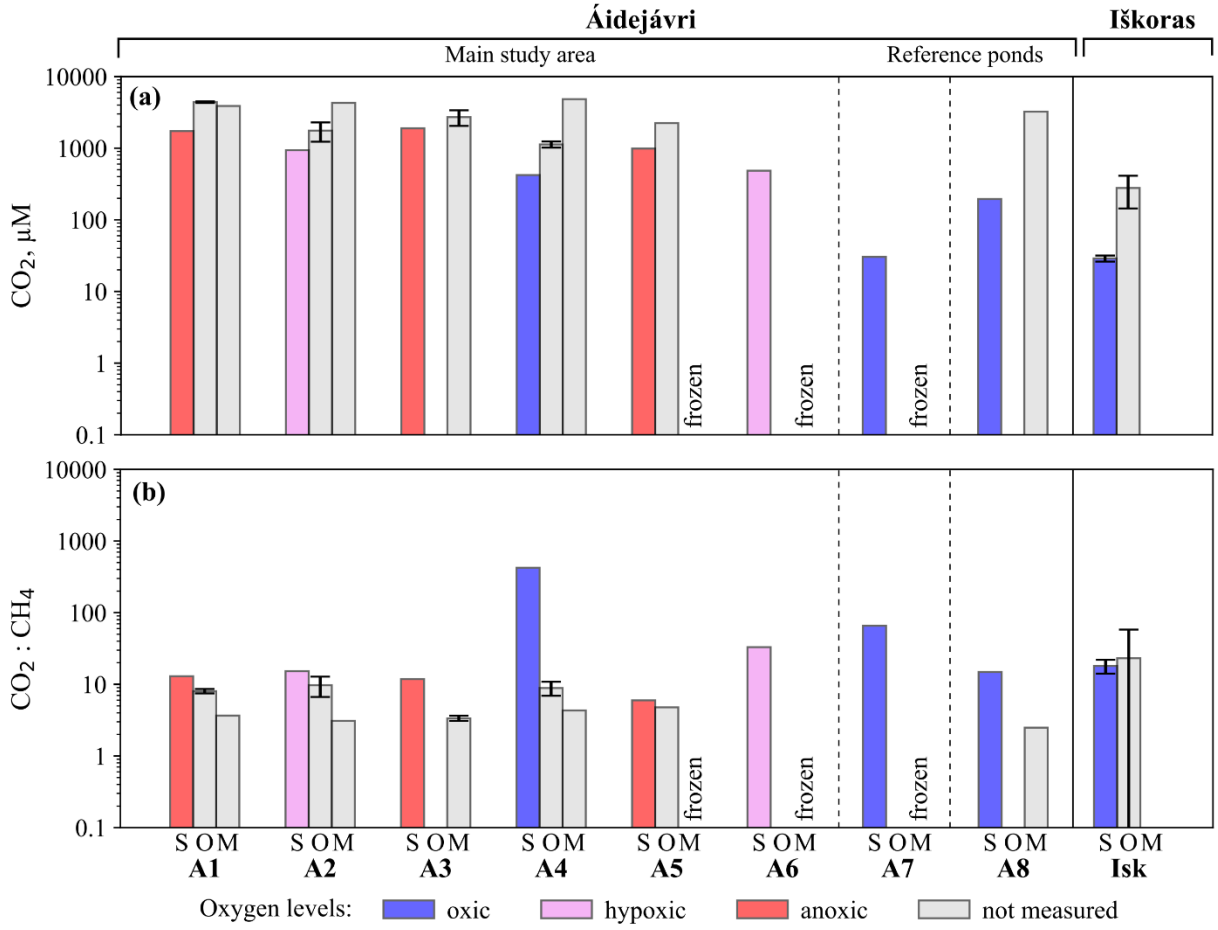

Figure S9. Dissolved CO_2 concentrations (a) and CO_2:CH_4 ratio (b) in the unfrozen water column of the studied ponds across each season (March - M, September - S, and October - O, 2024). Error bars represent the standard deviations of multiple samples (n = 3 - 12) collected from different depths in March and October, as well as replicate samples taken in September from the same depth. Note that the months are presented in non-chronological order to reflect the logical sequence of the winter CH_4 accumulation.

S2.2. CH_4 storage prior to freezing

To estimate the CH_4 storage prior to freezing (S_{prior}, Sect. 3.5, main text) we used CH_4 concentrations in the first winter ice layer formed which was sampled in March 2024 and in the water prior to freezing which was sampled in September 2024 (Fig. S10). CH_4 concentrations measured in September 2024 were adjusted to a water temperature of 0°C by applying solubility constants for 0°C

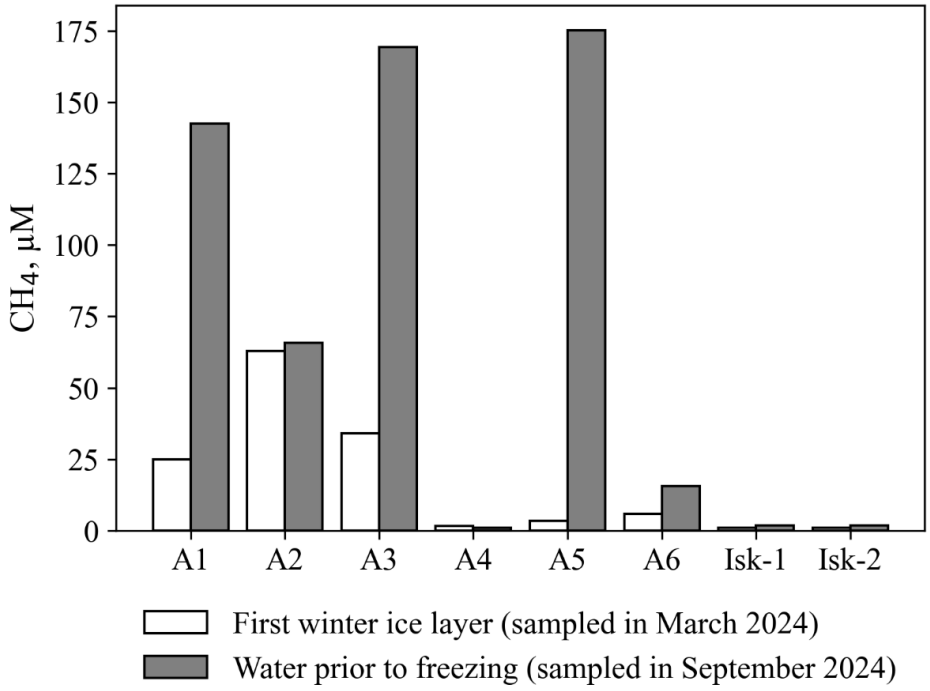

Figure S10. Mean CH_4 concentrations in the first winter ice layer formed (sampled in March 2024) and in the water prior to freezing (sampled in September 2024). September 2024 CH_4 concentrations were adjusted to the solubility at 0°C (Sect. 3.5, main text).

S2.3. pH and Dissolved Organic Content (DOC) of ice layers

pH values of ice layers ranged from 4.4 to 8.2 (Table S1). DOC concentrations ranged from 1.9 mg L^{-1} to 160 mg L^{-1} (Table S1, Sect. 4.1, main text).

Table S1. Mean pH and Dissolved Organic Content (DOC) of ice layers (Sect. 4.2, main text).

Ice core	Depth from, m	Depth to, m	Ice type	DOC, mg L^{-1}	pH
A1	0	0.06	Superimposed	22	5.2
	0.06	0.35	Clear ice	3.6	6.2
	0.35	0.49	Mixed bubbles	3.2	6.2
A2	0	0.13	Ebullition bubbles	3.8	6.6
	0.13	0.22	Spherical and nut shaped bubbles	3.0	6.5
	0.22	0.30	Spherical and nut shaped bubbles	5.4	5.9
	0.30	0.42	Mixed bubbles	3.0	6.1
	0.42	0.46	Mixed bubbles	3.8	5.8
A3	0	0.28	Superimposed	14	6.4
	0.28	0.36	Ebullition bubbles	4.0	6.2

	0.36	0.46	Clear ice	4.8	6.2
	0.46	0.53	Spherical and nut shaped bubbles	4.4	6.3
A4	0	0.25	Ebullition bubbles	3.3	6.0
	0.25	0.33	Mixed bubbles	3.2	6.0
	0.33	0.58	Mixed bubbles	4.4	5.9
A5	0	0.06	Superimposed	17	5.8
	0.06	0.15	Clear ice	3.1	6.1
	0.15	0.22	Spherical and nut shaped bubbles	36	4.9
	0.22	0.39	Mixed bubbles	8.7	5.2
	0.39	0.56	Frozen peat	110	4.4
A6	0	0.27	Superimposed	20	5.6
	0.27	0.40	Clear ice	4.1	5.9
	0.40	0.49	Mixed bubbles	160	4.6
	0.49	0.53	Frozen peat	150	4.4
A7	0	0.13	Clear ice	3.2	6.2
	0.13	0.28	Elongated bubbles	3.4	6.3
	0.28	0.42	Elongated bubbles	2.8	6.1
	0.42	0.58	Mixed bubbles	19	5.4
A8	0	0.06	Superimposed	7.4	8.1
	0.06	0.18	Clear ice	2.1	6.4
	0.18	0.29	Elongated bubbles	2.2	6.2
	0.29	0.45	Elongated bubbles	2.8	6.3
Isk-1	0	0.05	Superimposed	12	4.8
	0.05	0.15	Clear ice	4.6	5.6
	0.15	0.25	Mixed bubbles	3.5	5.6
	0.25	0.37	Mixed bubbles	67	5.0
	0.37	0.5	Mixed bubbles	115	5.3
Isk-2	0	0.06	Superimposed	18	4.9
	0.06	0.22	Clear ice	2.5	5.8
	0.22	0.26	Spherical and nut shaped bubbles	2.7	5.8
	0.26	0.42	Mixed bubbles	6.4	5.6
	0.42	0.55	Mixed bubbles	7.7	5.4

S2.3. CH_4 storage and fluxes during winter

The winter CH_4 bottom flux F_{winter} was calculated (Sect 3.6, main text) using the pond-derived winter CH_4 storage, including ice and below ice storages, as well as storage in the water column prior to freezing, S_{prior} (Table S2).

Table S2. CH_4 storages (prior to freezing, in the ice and below-ice) and calculated winter CH_4 bottom flux (Sect 3.6, main text).

	CH_4 storages, mg CH_4-C m^{-2}			Winter CH_4 bottom flux, F_{winter}, mg CH_4-C m^{-2} d^{-1}
	Water storage prior to freezing, S_{prior}	Ice storage	Below-ice storage	
A1	1307 ± 923	410 ± 64	10303 ± 1372	59 ± 11
A2	1121 ± 81	1521 ± 260	16626 ± 1874	106 ± 14
A3	1343 ± 901	297 ± 81	5524 ± 1008	28 ± 8.6
A4	14 ± 3	1114 ± 159	3347 ± 1349	28 ± 8.7
A5	418 ± 416	3349 ± 431	-	18 ± 3.9
A6	45 ± 24	422 ± 211	-	2.4 ± 1.3
A7	2.2 ± 1.3	846 ± 104	-	5.3 ± 0.7
A8	69 ± 67	281 ± 58	5474 ± 1588	36 ± 10
Isk-1	10 ± 4	514 ± 110	(1271 ± 1271) *	3.1 ± 0.7 (11 ± 8) *
Isk-2	11 ± 4	1719 ± 334	(636 ± 636) *	11 ± 2.2 (15 ± 4.6) *

*The values were estimated based on the assumption of dissolved methane storage under the ice in Iškoras pond (Sect. 3.5).

S2.4. CH_4 fluxes during summer

The ice-free surface-to atmosphere methane flux was measured by eddy covariance at the Iškoras site. CH_4 fluxes for the thermokarst ponds within the peat plateau complex were estimated from footprint analysis combined with machine learning (Pirk et al., 2024; Table S3).

Table S3. Mean CH_4 ice-free fluxes for ponds over three years (2019-2021) estimated by eddy covariance at the Iškoras site (Pirk et al., 2024). The ice-free period was defined as June 10 to September 10 to exclude contributions from ice melt and autumn turnover. The mean temperature of the pond during this period in 2023 was 11.4°C.

Year	Ice-free CH_4 flux, mg CH_4-C m^{-2} d^{-1}			
	mean	std	25th	75th
2019	37	20	24	49
2020	40	22	25	54
2021	39	20	26	53

References

Åberg, J. and Wallin, M.: Evaluating a fast headspace method for measuring DIC and subsequent calculation of pCO_2 in freshwater systems, IW, 4, 157–166, https://doi.org/10.5268/IW-4.2.694, 2014.

Knutson, J. K., Clayer, F., Dörsch, P., Westermann, S., and de Wit, H. A.: Water chemistry and greenhouse gas concentrations in waterbodies of a thawing permafrost peatland complex in northern Norway, Biogeosciences, 22, 3899–3914, https://doi.org/10.5194/bg-22-3899-2025, 2025.

Martin, L. C. P., Nitzbon, J., Scheer, J., Aas, K. S., Eiken, T., Langer, M., Filhol, S., Etzelmüller, B., and Westermann, S.: Lateral thermokarst patterns in permafrost peat plateaus in northern Norway, The Cryosphere, 15, 3423–3442, https://doi.org/10.5194/tc-15-3423-2021, 2021.

Maxim Integrated: DS1922L/DS1922T data sheet, https://www.analog.com/media/en/technical-documentation/data-sheets/ds1922l-ds1922t.pdf, (last access: 12 December 2025), 2015.

Norgeibilder.no: Statens kartverk, Geovekst og kommunene: Kautokeino 1958, Alta Kautokeino riksgrensen 1966, Roavvoaivi 2003, Finnmark 2013, Karasjok 2003, Finnmark 2011, https://www.norgeibilder.no/, last access: 3 June 2025.

Pirk, N., Aalstad, K., Mannerfelt, E. S., Clayer, F., De Wit, H., Christiansen, C. T., Althuizen, I., Lee, H., and Westermann, S.: Disaggregating the Carbon Exchange of Degrading Permafrost Peatlands Using Bayesian Deep Learning, Geophysical Research Letters, 51, e2024GL109283, https://doi.org/10.1029/2024GL109283, 2024.